Available online at www.sciencedirect.com
SCIENCE DIRECT®
Journal of Sound and Vibration 276 (2004) 45–63
JOURNAL OF SOUND AND VIBRATION
www.elsevier.com/locate/jsvi

Integrating experiments into an energy-based reduced-order model for vortex-induced-vibrations of a cylinder mounted as an inverted pendulum

P. Dong, H. Benaroya, T. Wei*

Department of Mechanical and Aerospace Engineering, Rutgers University, 98 Brett Road, Piscataway, NJ 08854-8058, USA

Received 6 September 2002; accepted 20 July 2003

Abstract

High-resolution digital particle image velocimetry has been used to measure fluid energy transport terms necessary for developing a scientifically rigorous Hamilton's Principle approach to modelling fluid–structure interactions. The interaction being modelled is the vortex-induced vibration of a low mass-damping circular cylinder mounted like an inverted pendulum in a water tunnel. Data in this paper are specifically focussed on the case where the cylinder undergoes large amplitude modulated oscillations slightly below the cylinder's natural frequency. This paper describes the experimental methodology used to acquire key modelling data, i.e. kinetic energy transport and work by viscous forces across the boundaries of an integral control volume. Integration of these data into the coupled energy equation is also described. The ability of this modelling approach to accurately capture complex phenomena such as beating is demonstrated.

1. Introduction

In an earlier work, Benaroya and Wei [1] presented a detailed formulation of a Hamilton's Principle approach to modelling fluid–structure interactions. The overall goal of the effort was to develop a scientifically based methodology for reduced-order modelling of the fully coupled response of a structure to complex fluid loading. In this paper, experimental contributions necessary for developing and validating such models are addressed. We begin with a review of the model equation and a discussion of the requirements for developing a robust, dynamically

*Corresponding author. Tel.: +1-732-445-2718; fax: +1-732-445-3124.
E-mail address: twei@jove.rutgers.edu (T. Wei).

0022-460X/$ - see front matter
doi:10.1016/j.jsv.2003.07.041

accurate model. This is followed by a description of experimental methodologies along with a presentation of energy transport measurements. Integration of experimental data into the reduced-order analytical model completes this paper.

1.1. A brief overview of analytical fluid–structure modelling

There is an extensive body of literature on analytical modelling of vortex-induced vibrations. This may be roughly divided into two categories: single-degree-of-freedom and coupled wake-oscillator models. Single-degree-of-freedom models use a single ordinary differential equation to describe the behavior of the structure oscillation. Wake dynamics are incorporated into the equation through the use of some appropriately defined forcing function. Coupled wake-oscillator models use two ordinary differential equations to simulate the fluid–structure system. One represents the structure while the other treats the periodic wake of the structure as an oscillator. It is important to note at the outset that, in order to fully understand the coupled interaction problem, the structure and fluid should not be separated. Flow characteristics depend on the structure's motion and vice versa. This will be addressed throughout this paper.

The principal advantage of single-degree-of-freedom models for vortex-induced-vibrations is simplicity. Structural response may be determined by solving a single equation of motion. For example, the equation of motion for a pendulum-like, linearly damped, and periodically forced cylinder can be expressed as

$$m\ddot{x} + c\dot{x} + kx = F, \tag{1}$$

where m, c, k, x and F are the cylinder's mass, linear material damping constant, spring constant, transverse displacement and aero/hydro-elastic forcing function, respectively. First and second time derivatives of x are denoted as $\dot{x}$ and $\ddot{x}$, respectively. Additionally note that $c = 2m\zeta\omega_n$ and that $k = m\omega_n^2$, where ω_n is the cylinder's natural frequency and ζ is the fraction of critical damping, or the damping factor. F generally takes the form of $F(x, \dot{x}, \ddot{x}, \omega_s, t)$ with ω_s representing the Strouhal frequency.

Single-degree-of-freedom models may be further subdivided into 'negative-damping' or 'forced-coefficient data' models. Negative damping models are generally applicable to freely vibrating structures. They are based on the assumption that aero/hydro-elastic damping effects may become strong enough to offset mechanical damping. When this is true, aero/hydro-elastic damping effectively introduces a negative-damping type instability. Examples of works using this modelling approach include Basu and Vickery [2] and Simiu and Scanlan [3].

An alternative approach within single degree-of-freedom modelling is to incorporate experimentally determined force coefficient data. The advantage of this is that fluid–structure couplings are introduced into the model, albeit simplistically and indirectly, through the use of experimental constants. For example, Sarpkaya [4] used force measurements from an externally excited cylinder to develop the expression, $F = \rho_r \Omega^2 (C_{ml} \sin \Omega\tau - aC_{dl} \cos \Omega\tau)$, where C_{ml} and C_{dl} were defined to be the inertia and drag coefficients, respectively.

Regardless of how it is done, accurately describing non-linear fluid–structure coupling within the framework of a single degree-of-freedom model is highly problematic. For this reason, coupled wake-oscillator models were introduced. Building on the work of Bishop and Hassan [5],

Hartlen and Curie [6] developed probably the most widely used coupled wake-oscillator model to date. In their model, a van der Pol-type soft non-linear equation for the lift force was coupled to the body motion by a linear dependence on cylinder velocity. The model equations were

$$\ddot{x} + 2\xi\dot{x} + x = a\Omega C_L \tag{2a}$$

and

$$\ddot{C}_L - a\Omega\dot{C}_L + (\gamma/\Omega)\dot{C}_L^3 + \Omega^2 C_L = B\dot{x}. \tag{2b}$$

In these equations, C_L was defined as the lift coefficient. Ω was the ratio of vortex shedding frequency, f_s, to the structure's natural frequency, f_n. ξ was the damping coefficient and a, γ and B were model constants.

Hartlen and Curie [6] assumed that the structure's displacement, x, and lift force coefficient, C_L, varied sinusoidally in time with a common frequency, f_c, i.e. the frequency of structural vibrations:

$$x = X \sin 2\pi f_c t, \tag{3a}$$

$$C_L = \overline{C_L} \sin(2\pi f_c t + \phi). \tag{3b}$$

Substituting these expressions into the model equations (2a) and (2b), Hartlen and Currie [6] obtained relations between f_s, f_c, the phase, ϕ, and maximum amplitude, X. Variants of the coupled wake-body model developed around the same time include Landl [7] and Iwan and Blevins [8].

Closer examination of the Hartlen and Curie model, particularly equation (3), clearly indicates the need for simplifying assumptions in order to implement the model. Depending on the assumptions, significant physical phenomena, including key couplings, may be overlooked. Indeed, as will be shown in this paper, the assumption of a single characteristic frequency, f_c, will not permit description of beating behavior. It is also not a simple matter to define X or $\overline{C_L}$ in a manner that reflects the coupled influence of fluid loading on structural response and vice versa. For these reasons, Benaroya and Wei [1] extended the modelling paradigm, introduced by McIver [9], to examine external flows around elastic structures.

1.2. The reduced-order energy-based equation of motion

One of the unique features introduced in Ref. [1] was the use of an integral control volume containing both the structure as well as a region of fluid surrounding the structure. The control volume may either be defined to move with the structure or to be stationary. In the latter formulation, the control volume must be large enough to accommodate the full range of motion of the structure without the structure crossing the control volume boundaries. For a control volume moving with the structure, the amount of fluid contained in the control volume can be made arbitrarily large or small as a function of mathematical or experimental expedience.

Regardless of the type of control volume chosen, the equation of motion derived in Ref. [1] may be written in the simplified form

$$\mathrm{d}/\mathrm{d}t\left\{\underset{1a}{T_{structure}}+\underset{1b}{T_{fluid}}+\underset{1c}{\Pi_{structure}}\right\}CV = \underset{2}{\int_{CS}[\rho U^2/2](\mathbf{U}-\mathbf{V}_{CV})\cdot\mathbf{n}\,\mathrm{d}s}+\underset{3}{\int_{CS}(-p\mathbf{n}+\boldsymbol{\tau})\cdot\mathbf{U}\,\mathrm{d}s}. \quad (4)$$

Here, T denotes kinetic energy, Π represents potential energy, $\frac{1}{2}\rho U^2$ is the kinetic energy of the fluid motions, $\mathbf{U}$ and $\mathbf{V}_{CV}$ are the instantaneous local fluid and control surface boundary velocity vectors, respectively, and finally, p and $\boldsymbol{\tau}$ are pressure and the viscous stress tensor, respectively. The unit outward normal vector is denoted as $\mathbf{n}$, and the subscripts CV and CS indicate volume or boundary surface integration. In Ref. [1], the control volume was divided into a *closed* region containing the structure, and an *open* region containing the fluid immediately surrounding the structure. For simplicity, these two regions are combined here so that the integrals on the right-hand side of Eq. (4) may be considered to contain both *closed* and *open* regions.

Eq. (4) is an integral formulation of the mechanical energy transport equation for a control volume containing both the structure and a region of fluid immediately surrounding the structure. The left-hand side includes time derivatives of kinetic and potential energies of the structure, 1a and 1c, and temporal variations of the fluid kinetic energy, 1b. These comprise the time rate of change of mechanical energy in the control volume at any instant of time. Terms on the right-hand side of Eq. (4) include the net flux of fluid kinetic energy across the boundaries of the control volume, term 2, and work done on the control volume boundaries by pressure and viscous forces, term 3, i.e. the non-conservative surface forces. These are effectively the fluid 'forcing' functions for the structure terms on the left-hand side of Eq. (4).

1.3. Using experimental data as model input

A fundamental challenge facing any fluid–structure interaction modeller is accurately describing the fluid forcing. For the one equation model, Eq. (1), an expression for F is required. Eq. (2) requires an expression for C_L while Eq. (4) requires time-dependent expressions for fluid kinetic energy flux and rate of work. Depending on approach, there are frequently tradeoffs required in formulating a fluid–structure interaction model. In analytical modelling, there is often a mathematical tradeoff required between mathematical accuracy and tractability. Further, if experiments are to be used, the type of data that can be obtained, particularly for a complex geometry, often limits the modeller. For example, wake-oscillator models use lift coefficient data with assumed sinusoidal variations in time.

Advances in fluid measurement techniques over the past decade have created opportunities to significantly advance the modelling process. In a series of studies including, Shah et al. [10], Hsu et al. [11] and most recently, Grega et al. [12] we have been able to employ high-resolution digital particle image velocimetry (DPIV) to examine complex derivative quantities in turbulent flow. These include examination of vorticity transport and strain across a turbulent trailing vortex from a half delta wing; Shah et al. [10]. Terms in the differential turbulent kinetic energy and vorticity transport equations were presented for a turbulent boundary layer in water interacting with a free

surface in Hsu et al. [11] and Grega et al. [12]. In light of these advances, there is no longer a need to limit experimental input to the models to the most fundamental of measurable quantities such as C_L. Neither is it necessary to superimpose such a high degree of simplification to the experimental data such as constant amplitude sinusoidal variations in the forcing functions. Our approach in this investigation has been to develop a reduced-order analytical fluid–structure interaction model incorporating temporally and spatially resolved DPIV measurements of the fluid 'forcing'; terms 2 and 3 in Eq. (4). By accurately measuring the fluid forcing terms, we effectively use experiments to 'derive' a set of 'analytical' expressions for the fluid forcing. There would be no assumptions inherently built into the model. It is important to note at the outset, however, that DPIV is 'only' a two-dimensional, velocity field measurement technique; for a detailed uncertainty analysis for the present measurement system, please see Grega et al. [12]. Discussions of current limitations and possible solutions are included at appropriate points.

2. The oscillating cylinder

The model problem addressed in this study was the vortex-induced vibration of a low mass-damping-ratio circular cylinder mounted as an inverted pendulum. The cylinder was restrained at its bottom end by a stainless-steel pin but restricted to move in the cross-stream plane only. A schematic drawing of this model problem is shown in Fig. 1. One can think of the dynamics as an inverted pendulum excited by its own periodic vortex shedding. For the purposes of this analysis, the amplitude of motion of the free, upper end was sufficiently small that the flow could be considered to be nominally two dimensional. Indeed the model results will verify this assertion. Three-dimensionality effects have been examined by Voorhees [13] and will be presented in a separate paper.

The structure used in this study was a 2.54 cm diameter (D) cylinder constructed of thin, 0.16 cm, wall acrylic tube. It was 128 cm long and immersed in a uniform flow of water, $\sim$107 cm deep. Acrylic was used to facilitate optical access completely around the structure by permitting the DPIV laser illumination sheet to pass through the structure, i.e. there was very little shadow cast by the cylinder opposite the light source. In Ref. [1], an aluminum cylinder was used which did not permit measurement throughout a shadow region upstream of the cylinder.

To further minimize refraction effects as laser light passed through the cylinder, a 2.54 cm long $\times$ 2.22 cm diameter plug was installed close to the cylinder mid-height and a small amount of water, $\sim$2.54 cm deep, was placed in the cylinder above the plug. The plug was fitted with o-rings so that it could be positioned wherever needed along the cylinder's length. In this case, the plug was positioned $\sim$70 cm from the bottom of the cylinder. The total mass of the plug and water was negligible in relation to the total structural mass, but it effectively allowed transmission of the DPIV laser illumination sheet through the cylinder with minimal distortion.

As noted earlier, the cylinder was mounted to the floor of the Rutgers Free Surface Water Tunnel facility using a 0.32 cm diameter stainless-steel pin; both ends of the pin were threaded. The top end of the pin was secured to the bottom of the cylinder using a second plug, 2.22 cm in diameter and 3.81 cm in length. The bottom end of the pin was screwed to a 1.27 cm thick base plate. The effective length of the pin after installation was 5.08 cm. In order to minimize end effects, the second plug was inserted up inside the cylinder with its bottom face $\sim$2.54 cm above the bottom of the cylinder. A $\sim$2.54 cm clearance between the bottom of the cylinder and the base plate was left in order to prevent contact as the cylinder oscillated.

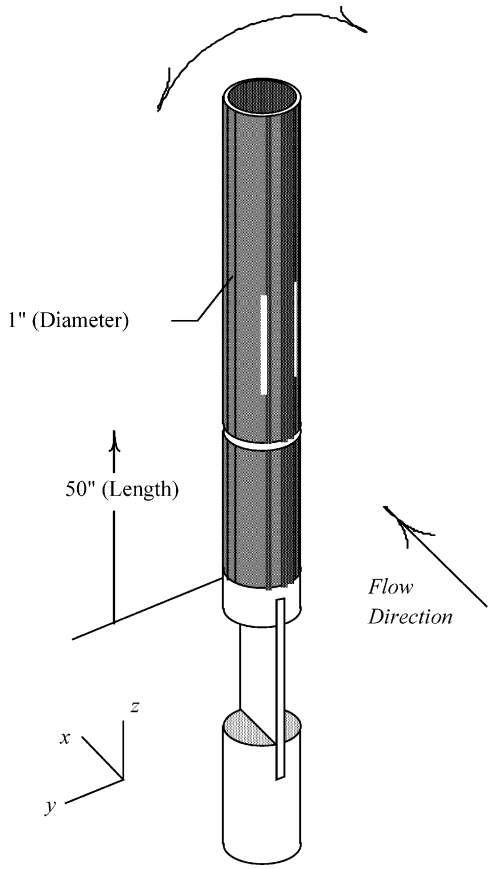

Fig. 1. Schematic drawing of one of the oscillating cylinder experiment, hollow aluminum tubes with leaf spring attachment. Observe that the bottom end was fixed to the water tunnel floor by the leaf spring while the top end was free to move. The principal differences between the aluminum and acrylic cylinders were the transparency of the acrylic and the use of a stainless-steel pin at the acrylic cylinder base instead of a leaf spring.

To ensure motion was restricted to the cross-stream plane a cart/track assembly was placed on the free end of the cylinder protruding through the free surface. This is shown in Fig. 2. The cart was simply a block of PVC with a 2.54 cm diameter hole in its center, fitted with two pairs of ball bearings on opposing faces. This cart was constrained to move between two polished steel plates which were rigidly mounted above the free surface and oriented in cross-stream planes. The friction resistance of this cart assembly was minimal.

In this study, the cylinder as modelled as a simple harmonic oscillator with frictional damping. The model equation was

$$\frac{1}{2}\frac{\mathrm{d}}{\mathrm{d}t}[I_0\dot{\theta} + k_T\theta^2 - (mg - B)L\cos\theta] = \int_{CS}[\rho U^2/2](\mathbf{U} - \mathbf{V}_{CV})\cdot\mathbf{n}\,\mathrm{d}s + \int_{CS}(-p\mathbf{n} + \boldsymbol{\tau})\cdot\mathbf{U}\,\mathrm{d}s. \quad (5)$$

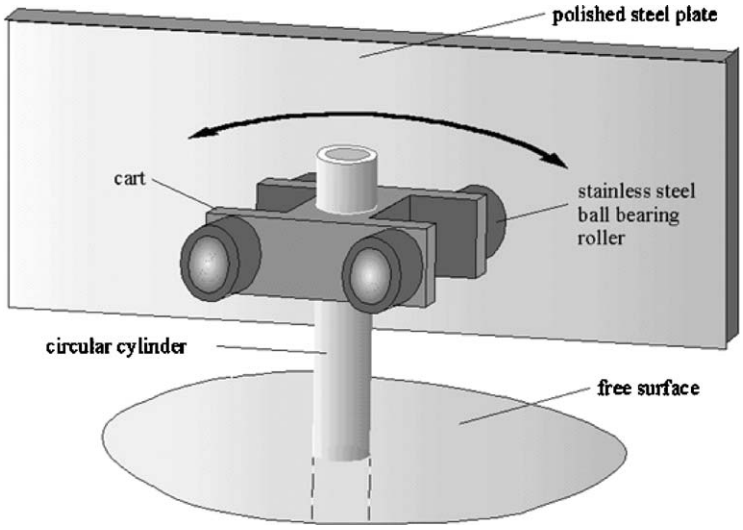

Fig. 2. Detailed schematic showing the cart and track assembly used to restrict cylinder motion to the cross-stream plane.

One should recognize this as a specific form of Eq. (4) where I_0 is the moment of inertia for the total structure (including cart, plugs, etc.), $k_T = I_0(2\pi f_n)^2$ is the structure's stiffness, m is the total structural mass, g the gravitational constant, B the net buoyancy of the structure and L the total length. The cylinder's angular deflection is denoted by θ. Note that k_T may also be interpreted as an effective linear torsional spring constant of the stainless-steel pin. The right-hand side of Eq. (5) contains the identical fluid kinetic energy flux and rate of work terms identified for Eq. (4).

The mass-ratio, m^*, of the cylinder was 0.65, where m^* is defined as the ratio of the structure's total mass to the mass of water displaced by the structure. The cylinder's damping ratio, ζ, was 0.058. Its natural frequency, f_n, was 0.83 Hz in air and 0.77 Hz in water. The total moment of inertia for the entire cylinder assembly, I_0, was 0.40 kg m^2. The stiffness of the structure, k_T, was 11.0 N m/rad. Note that the maximum angular deflection, θ_{max}, was 1.5°. This is consistent with the assertion that three-dimensional effects may be neglected. As noted earlier, Voorhees [13] demonstrated that for this experiment, Kármán vortices remained continuous along the entire length of the cylinder and that three-dimensional effects were dominant primarily at the free surface.

The frequency and amplitude response characteristics of the cylinder are shown in Figs. 3 and 4, respectively. Measurements were made at the cylinder mid-height, $\sim$70 cm above the floor of the water tunnel. Two plotter symbols, squares and diamonds, appear in both figures. The diamonds denote data taken while incrementing upward through the velocity range. Squares denote frequency and amplitude measurements made while decrementing downward through the speed range. Examining the cylinder response both while progressing through the speed range in both directions provided insight into any hysteresis that may be present in the system. It is also worth noting that when vortex-induced-vibrations occurred, both the cylinder oscillation and Kármán vortex shedding frequencies were identical when averaged over long sampling periods, i.e. 5–10 min.

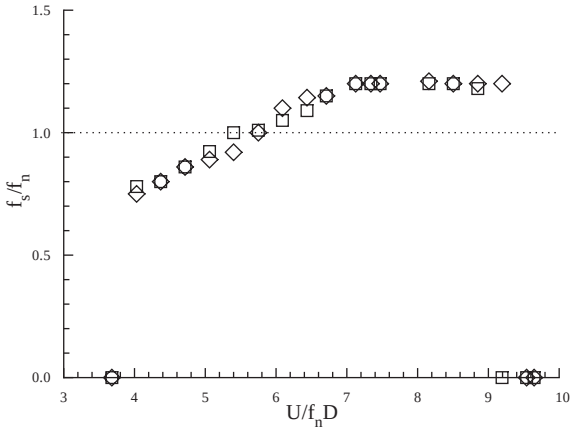

Fig. 3. Dimensionless cylinder oscillation frequency, f_0/f_n, vs. reduced velocity, Uf_n/D. Squares denote measurements taken for incrementally increasing speeds while diamonds indicate data taken while decreasing through the speed range.

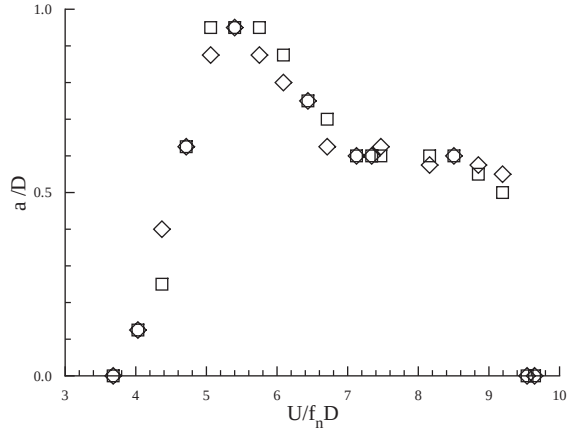

Fig. 4. Maximum amplitude response characteristics of the acrylic cylinder undergoing vortex-induced-vibrations. See caption Fig. 3 for definition of plot symbols.

A salient feature of the cylinder response characteristics is the existence of two distinct types of fluid–structure interaction. At the low speed end, $3.6 \leqslant U/f_nD \leqslant 6.4$, the interaction was characterized by strong energetic vortices shed very close to the cylinder and by a beating behavior of the cylinder oscillations. This was referred to as 'resonant synchronization' in Atsavapranee et al. [14] and as the 'upper branch' in Khalak and Williamson [15]. The maximum amplitude in the resonant synchronization regime occurred at $U/f_nD \approx 5.5$.

At higher speeds, $6.4 \leqslant U/f_nD \leqslant 9.0$, classic lock-in behavior could be observed. In this regime, cylinder oscillation frequency and amplitude remained constant over a wide range of flow speeds. Khalak and Williamson [15] refer to this as the 'lower branch' of the cylinder amplitude response curve. Flow visualization studies presented in Atsavapranee et al. [14] and Voorhees [13] indicated that in the classic lock-in regime, vortex shedding appeared rather disorganized in comparison to

the resonant synchronization regime. We interpreted this as the cylinder modulating the flow so that 'just enough' energy was transferred from fluid to structure to maintain a fixed amplitude oscillation at the natural frequency.

3. Experimental apparatus and methods

We now turn to the experimental methodology issues necessary to bring about a reduced-order analytical solution for this problem. Much of this was outlined in Ref. [1]. Detailed discussions of the flow facility, in-house DPIV system and measurement uncertainties may be found in Refs. [10,12]. Brief descriptions are included here.

Experiments were conducted in the Rutgers Free Surface Water Tunnel. The test section measured 58.4 cm in width $\times$ 122 cm in depth $\times$ 610 cm in length. It was constructed entirely from 1.91 cm thick glass panels for maximum optical access. With the test section completely filled, the maximum flow rate corresponded to a mean free stream velocity of approximately 30 cm/s. Free stream turbulence levels were less than 0.1% of the mean free stream velocity and the flow was uniform across the cross section to within $\pm 2\%$.

High-resolution DPIV measurements were made using a Kodak Megaplus ES1.0 video camera. The flow was seeded with 13 μm diameter silver coated glass spheres and illuminated using a New Wave Research Gemini PIV double-pulsed Nd:YAG laser. DPIV vector fields were computed from successive video images using a two-step spatial cross-correlation algorithm developed in-house. A sample instantaneous vector field is shown in Fig. 5 along with three of the integral control volumes examined. Again, an uncertainty analysis for velocity and velocity derivatives have been presented in Ref. [12]. As will be seen in the following section, the resolution and accuracy of the measurements enabled accurate assessment of terms 2 and 3 in the energy Eq. (4).

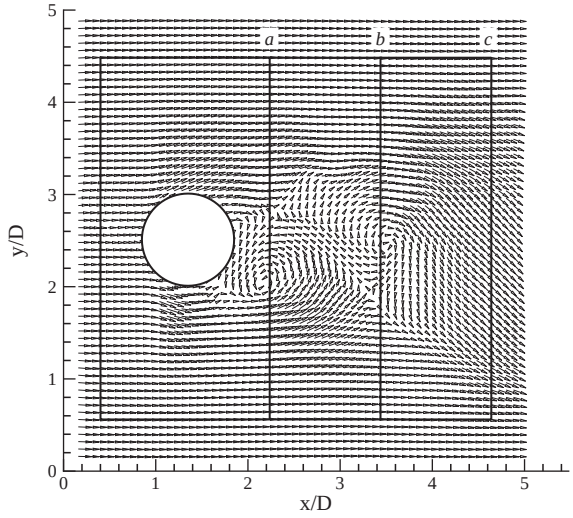

Fig. 5. Instantaneous DPIV vector field showing flow around the acrylic cylinder. Flow is left-to-right. Three of seven control volumes are shown including the smallest (a) and largest (c). Modelling was done using volume (b).

Records of instantaneous cylinder position were measured using a Banner Omni-beam OASBD analog photoelectric sensor. The sensor operated on the principle of measuring the reflected intensity of an 880 nm infrared source beam. A small white reflecting surface was attached to the top of the cylinder to improve signal quality. Output from the position sensor was transferred to a PC through a 12-bit analog to digital A/D board. Cylinder position data were captured at 100 Hz, 10 times faster than the DPIV sampling rate. This ensured clean accurate position information each time flow data were acquired.

4. DPIV measurements

In this section, we examine the process of incorporating time resolved DPIV data into a reduced order analytical model. The $Re = 2300$ case, in the resonant synchronization regime, was chosen because of the high degree of synchronization between vortex shedding and cylinder motion. This corresponds to the diamond shaped data point at $U/f_nD \approx 4.4$ and $a/D \approx 0.4$ in Fig. 4.

The data set consisted of an ensemble of 50 sets of 225 consecutive DPIV velocity field measurements taken at 100 ms intervals, or $\sim\frac{1}{12}$ of a cylinder oscillation period, in a horizontal plane perpendicular to the axis of symmetry of the cylinder at rest. The location of the measurement plane was ~ 70 cm above the floor of the test section coinciding with the amplitude measurements. The spacing between vectors was 0.19 cm corresponding to $\lambda/D = 0.074$. The total duration of the sample was 22.5 s, or approximately 17 cylinder oscillation periods.

The first step in providing experimental support for the modelling effort was to compute integral quantities in Eq. (4), i.e. terms 1b, 2, and 3, from each of the 225 instantaneous vector fields. Structural energy terms, 1a and 1c, were obtained from the optical position sensor output. DPIV vector fields could be temporally matched to the cylinder position vs. time trace because the cylinder position could also be determined directly from the video images. Examples of energy transport contour plots at different times in a cylinder oscillation cycle were shown in Benaroya and Wei [1].

Seven different sized control volumes were tested in this study as described in Ref. [16]. Three of the control volumes are shown in Fig. 5. All seven share a common upstream face and common transverse faces (top and bottom faces in Fig. 5). The only difference was the x-locations of the downstream faces. The smallest and largest volumes tested are labeled in Fig. 5 as 'a' and 'c', respectively. The intermediate sized control volume labeled 'b' is the one for which model results are presented later in this paper. There were two additional control volumes between 'a' and 'b' and an additional two whose downstream faces were equally spaced between 'b' and 'c'. The dependence on control volume size and location is discussed later in this section.

Except for the pressure work term, appearing as part of term 3 in Eq. (4), terms in the integral mechanical energy transport equation could be calculated relatively easily from the DPIV data and from the cylinder position sensor signal. Spatial derivatives needed for the rate of viscous work term were computed using central differences. The time derivative of fluid kinetic energy, $\mathrm{d}T_{fluid}/\mathrm{d}t$, was computed by differentiating successive DPIV vector fields. The flux of fluid kinetic energy past a point could be computed directly using the measured velocity components at that point.

Computing pressure work could be done in two independent ways. Following the approach described in Ref. [17], it was in principle possible to compute instantaneous local pressure

gradients from the two-dimensional Navier–Stokes equations using a quasi-two-dimensional assumption. Pressure work could then computed directly from the DPIV measurements. The difficulty with this approach turned out to lie in prescribing a verifiable pressure boundary condition somewhere in the measurement field-of-view.

An alternative approach was to compute the residual of all of the other terms in Eq. (4). This method has the advantage of not needing a pressure boundary condition, but potentially suffers from error propagation if measurement uncertainties are high. Both approaches were examined for this investigation. A comparison of the two techniques is presented in Ref. [16]. In brief, we were able to compute traces of pressure work to within a dc constant. The offset was attributable to not being able to define a pressure boundary condition. For this reason, we chose to use the results of the second approach, computing the residual of all other terms in Eq. (4).

Computing integrals for a desired control volume, then, simply required summing values along a predetermined control volume boundary. The control volume used for this exercise is volume 'b' shown in Fig. 5. The upstream and downstream faces were $\sim\frac{3}{4}$ diameters upstream and two diameters downstream of the cylinder axis, respectively. By using a clear acrylic cylinder, it was possible to measure flow velocities around the structure, thereby placing the structure entirely within the control volume.

To remove the effects of small-scale fluctuations, e.g. shedding of Bloor vortices (for details, see Bloor [18] or Wei and Smith [19]), phase averaging was performed. Fifty sets of 225 vector fields were included in the ensemble. The cylinder position vs. time signal was used to line up individual data sets. Phase averaging was done by centering on the peak of a beat cycle. For further details, see Dong [16].

In principle, results from the reduced-order analytical model should be independent of control volume size and location as long as the structure remains within the control volume boundaries at all times. However, certain control volumes provide energy transport traces that are more readily interpreted. This can be seen by comparing phase averaged energy traces for different control volumes.

Figs. 6–8 include phase-averaged time histories of fluid energy transport terms obtained from the DPIV data for the three control volumes shown in Fig. 5. Fig. 6 shows traces from the smallest control volume, 'a', while Figs. 7 and 8 include energy traces from the intermediate and largest control volumes, 'b' and 'c', respectively. There are five traces in each figure representing terms in Eq. (4); the time rates of change of kinetic and potential energies of the cylinder, 1a and 1c have been combined into single traces in each figure appearing as dotted lines. The time rate of change of fluid kinetic energy in the control volume, term 1b, appear as solid black lines. The flux of fluid kinetic energy across the boundaries of the control volume is shown as solid gray lines. The horizontal dashed lines, appearing along the abscissae, are actually the rate of work done by viscous forces on the control volume boundaries. It makes sense that this term is negligibly small, as vortex shedding from cylinders is known to be a pressure driven flow. Finally, the dashed gray lines are the rate of work done by pressure forces on the boundaries of the control volume. All data in Figs. 6–8 have been non-dimensionalized by $\frac{1}{2}\rho U_\infty^3 L$, where '$L$' is the length of the upstream (or downstream) face of the control volume. This non-dimensionalization may be physically interpreted as the total kinetic energy flux of the free-stream flow into a control volume with upstream dimension, L. For these experiments, L was $\sim$10 cm and U_∞ was $\sim$9.5 cm/s.

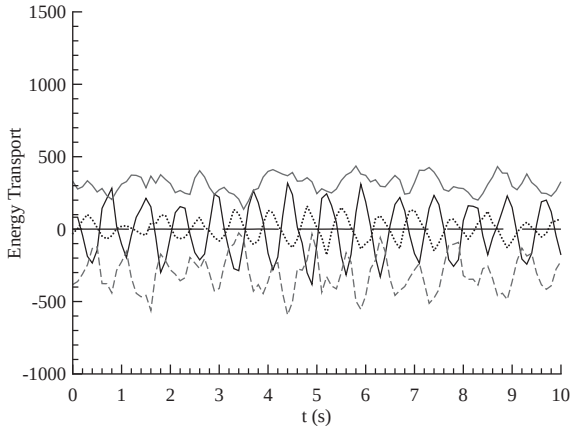

Fig. 6. Phase-averaged terms in the integral energy transport equation for the smallest control volume, 'a', in Fig. 4: ——, time rate of change of fluid kinetic energy in the control volume ($\partial KE/\partial t$); ——, flux of fluid kinetic energy across the control volume boundaries; — —, rate of work done by viscous forces; ……, time rate of change of mechanical energy of the cylinder ($\partial[KE + PE]/\partial t$); – – –, rate of work done by pressure forces calculated from the energy balance.

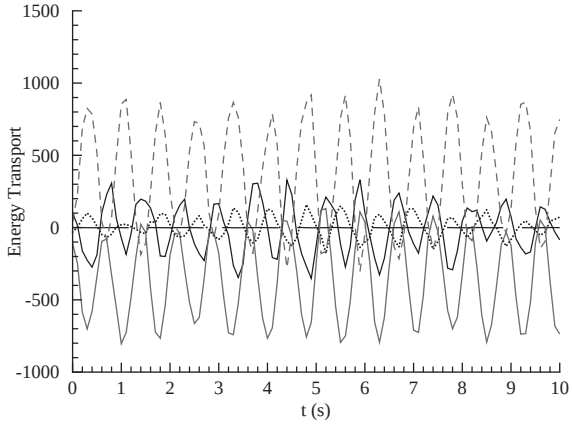

Fig. 7. Phase-averaged terms in the integral energy transport equation for the intermediate control volume, 'b', in Fig. 4. See Fig. 6 for plot legend.

Comparison of corresponding traces between Figs. 6–8 demonstrates the advantage of control volume 'b' over the other two. It should be intuitively obvious that the lateral faces of the control volume should have little impact on the energy transport signals (assuming, of course, that they are located far enough away from the mean cylinder mid-line to effectively be in the free stream). Because of the proximity of the upstream face to the cylinder, the flow into that face was not steady and uniform; integration along this face did contribute to the overall unsteadiness in the different energy transport terms. However, the dominant contributions to the surface integrals resulted from unsteady fluctuations in the cylinder wake. As such, it was the location of the downstream face that determined the magnitudes and form of the energy traces.

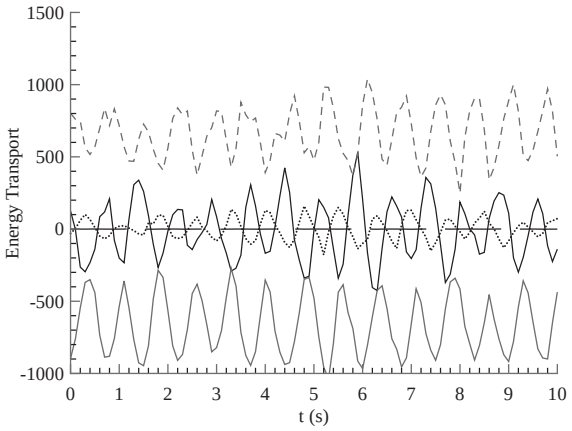

Fig. 8. Phase-averaged terms in the integral energy transport equation for the largest control volume, 'c', in Fig. 4. See Fig. 6 for plot legend.

Data from the smallest control volume appears in Fig. 6. One can clearly see that the fluid energy traces are quite irregular, particularly for the fluid kinetic energy flux. This is because the downstream face of the control volume lies inside the stagnation, or vortex formation region of the wake. This region is relatively insensitive to the strongly periodic velocity fluctuations associated with the Kármán vortices.

Strongly periodic signals were generated for control volume 'b', as shown in Fig. 7. The downstream face of this control volume was located immediately downstream of where the Kármán vortices rolled up and were shed from the cylinder. One would therefore expect that the fluid energy transport terms, particularly the fluid kinetic energy flux term, to be much more sinusoidal in form.

As Kármán vortices advect downstream away from the cylinder, viscous and turbulent diffusion becomes more prominent. In addition, complex vortex interactions, both on the small and large scales begin to deform the vortices. For descriptions of the various vortex interactions that may occur, the reader is referred to Wei and Smith [19], Williamson [20] and Voorhees [13]. As these phenomena develop, the energy transport signals become less sinusoidal. This can be seen in Fig. 8 for control volume 'c'. The downstream face of this control volume is located ~ 3 diameters downstream of the cylinder axes. Observe that while the phase-averaged traces are still quite periodic, they are not as clean as their counterparts in Fig. 7.

It is interesting to note, in comparing Figs. 6–8, that the 'dc' levels of both the fluid kinetic energy flux and pressure work terms change significantly as the downstream face of the control volume is varied. Indeed, observe that the kinetic energy flux term is positive in Fig. 6 for the smallest control volume and negative for the largest control volume, shown in Fig. 8. In Fig. 7, the flux term is predominantly negative, but with positive maxima.

Insight into why this happens can be seen in the sequence of contour plots shown in Fig. 9. Each of the eight double contour plots show instantaneous streamwise velocity, appearing as solid black lines superimposed on color contours of instantaneous fluid kinetic energy. Flow is left-to-right and the time between successive plots is 200 ms, i.e. every other vector field. The total duration of the sequence is 1.40 s, spanning slightly more than one cylinder oscillation period.

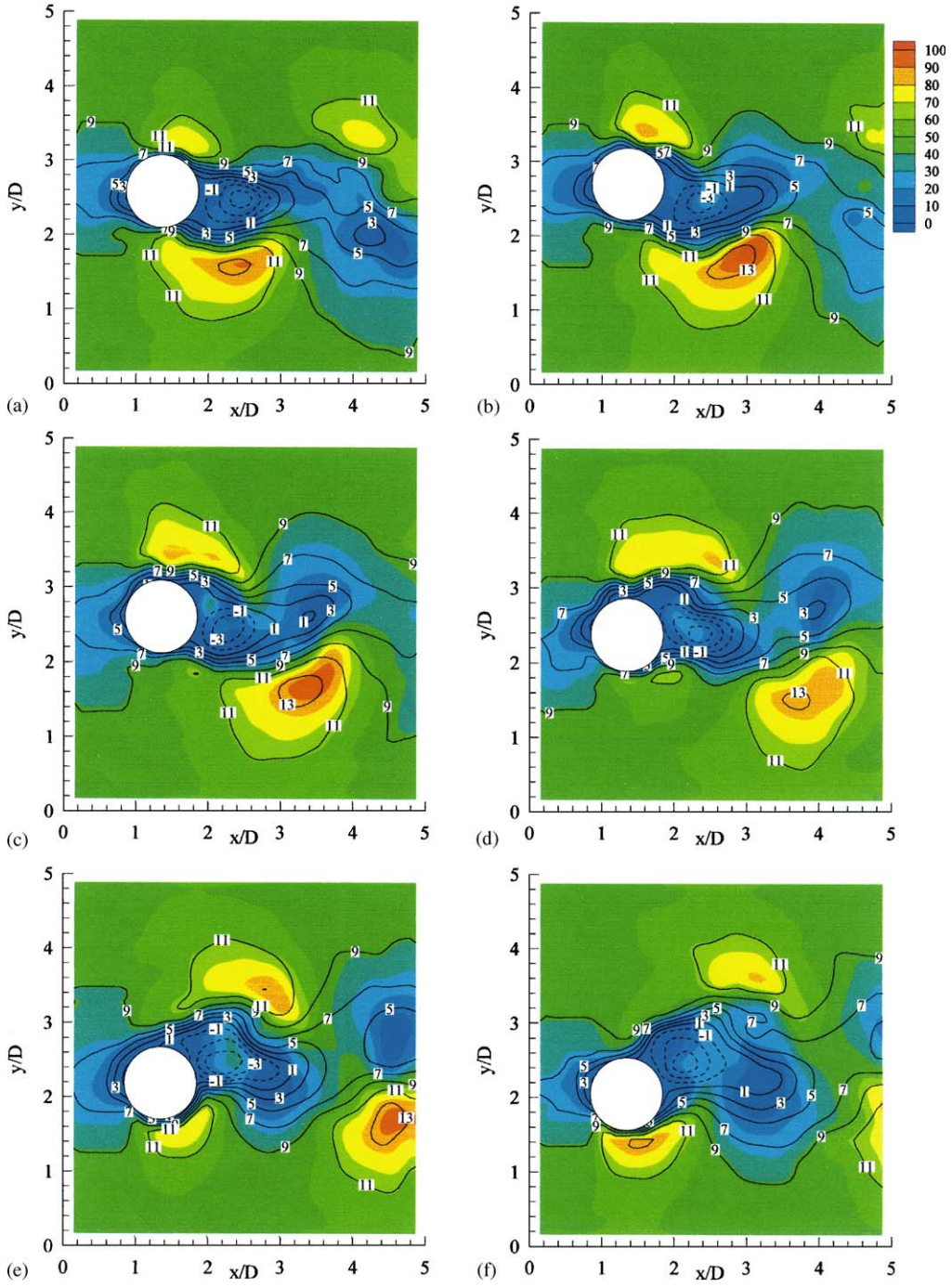

Fig. 9. Sequence of eight instantaneous measurements spanning one cylinder oscillation from data shown in Figs. 6–8. The time between successive plots is 200 ms. The flow is from left-to-right. Color contours denote instantaneous local fluid kinetic energy while line contours show magnitude of streamwise velocity. Quantities are dimensional (cm/s and cm^2/s^2).

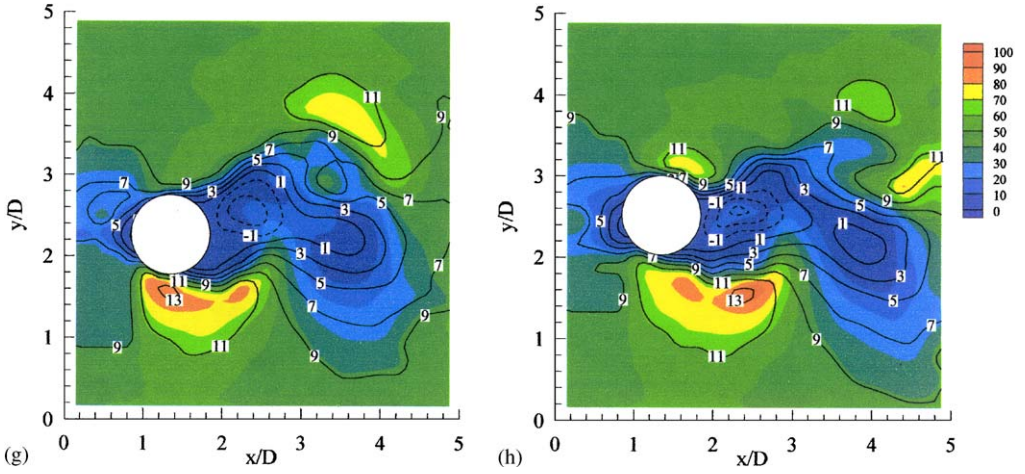

Fig. 9 (*continued*).

In looking at Fig. 9, one must recall that both the fluid kinetic energy flux and rate of work done by pressure forces include the product of energy (i.e. fluid kinetic energy, $\frac{1}{2}\rho U^2$, or potential energy, $-p$) with velocity normal to the local control surface. That is, the instantaneous flux of fluid kinetic energy in the stream direction at any point in the flow is the product of the kinetic energy and streamwise velocity at that point. In addition, we have previously addressed the importance of contributions from the downstream face of the control volume to the energy transport signals. With these two points in mind, it is instructive to look at the streamwise velocity contours with increasing distance from the cylinder trailing edge.

In particular, observe that $U<0$ immediately behind the cylinder, i.e. for $1.8 \leqslant x/D \leqslant \sim 2.6$, for every contour plot in Fig. 9. Farther downstream, however, $U > 0$ for $x/D > 2.6$. We attribute the variable 'dc' shift in fluid kinetic energy flux and pressure work as a reflection of the fact that flow immediately behind the cylinder actually moves upstream. When the downstream face of the control volume is sufficiently far downstream, kinetic energy flux and pressure work are uni-directional across the entire face.

5. Applying experiments to the reduced order analytical model

In the preceding section, we presented detailed flow measurements from an inverted oscillating pendulum experiment. The culmination of the analysis was a set of time traces of integral energy transport terms for a control volume surrounding the structure and some volume of fluid around the structure. In this section, we show how these data were applied to Eq. (4) and compare the reduced-order model of cylinder motion with the actual, experimentally measured oscillations.

The precise form of the equation of motion used in this analysis appears as Eq. (5). The structure was modelled as a damped rigid simple harmonic oscillator fixed at the base by a torsional spring. Properties of the structure were chosen to match that of the physical experiment. For details, the reader is referred to Ref. [16] or Ref. [21].

Eq. (5) was simulated using MATLAB in which the fluid forcing terms, terms 1b, 2 and 3, were the experimentally determined functions shown in Fig. 7. Since the data were obtained at discrete $\frac{1}{15}$ s intervals, a fast Fourier transform was performed on the data within MATLAB. Transforms of the four fluid energy transport terms for the intermediate control volume are shown in Fig. 10. These transforms may be interpreted as 'experimentally derived analytical expressions' for the fluid forcing. The unique feature of this approach is that we have directly measured terms in the governing equation requiring modelling. Except for quasi-two dimensionality, no empirical assumptions were incorporated into the model.

Inclusion of the transform data shown in Fig. 10 into Eq. (5) permitted solution for the time dependent cylinder position. A comparison between the actual cylinder motion and the motion predicted by our reduced-order model is shown in Fig. 11. An experimental, phase-averaged cylinder position vs. time trace is shown as a solid black line superimposed on the reduced-order model result, appearing as a dotted trace. The ordinate and abscissa are shown in dimensional form. Clearly, the agreement between model and experiment is quite good. Observe that both oscillation frequency and amplitude appear to be accurately predicted by the model along with the beating behavior. Numerical instabilities resulting from singularities when the cylinder was at points of maximum deflection are responsible for the clipping of the model result.

Careful examination of the spectra in Fig. 10 indicate a slight frequency mismatch between fluid kinetic energy flux and pressure work terms on one hand, and the time rate of change of the fluid kinetic energy term on the other. One can see from the individual spectra that the flux and work terms oscillate at a slightly lower frequency than the time derivative term. One can use physical arguments coupled with detailed study of the signals in Fig. 10 to conclude that fluid kinetic energy flux and pressure work correlate with the vortex shedding while changes in fluid kinetic energy around the cylinder follow the cylinder oscillation. Thus, we conclude that the beating phenomena observed in the resonant synchronization regime results from the competition between vortex shedding and structural vibration.

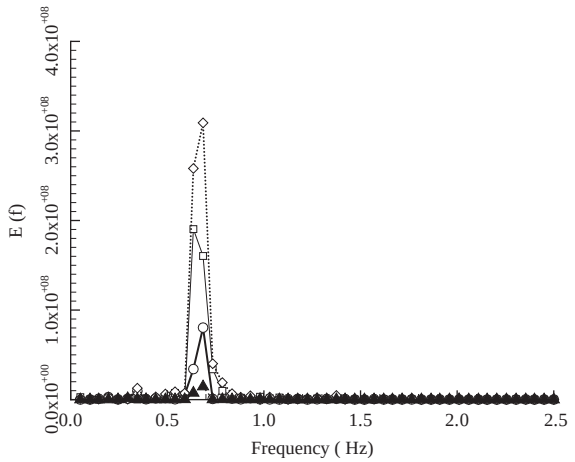

Fig. 10. Spectra of the fluid energy transport traces shown in Fig. 7. — ○ —, time rate of change of fluid kinetic energy in the control volume ($\partial KE/\partial t$); ⋯ ◇ ⋯, flux of fluid kinetic energy across the control volume boundaries; –□–, rate of work done by pressure forces; – – △ – –, time rate of change of mechanical energy ($KE + PE$) of the cylinder.

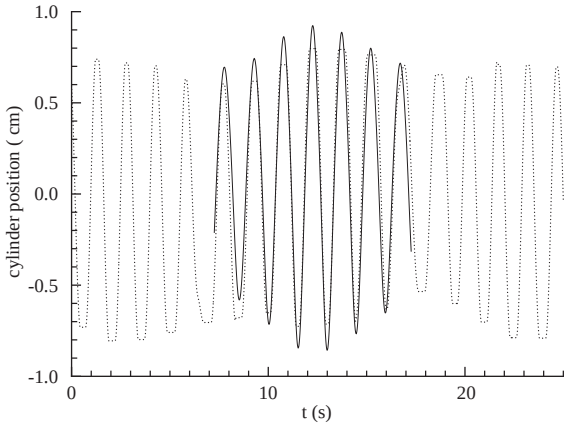

Fig. 11. Comparison of reduced-order model response (dotted line), for energy traces shown in Fig. 7, with phase-averaged cylinder position vs. time measurements (solid line).

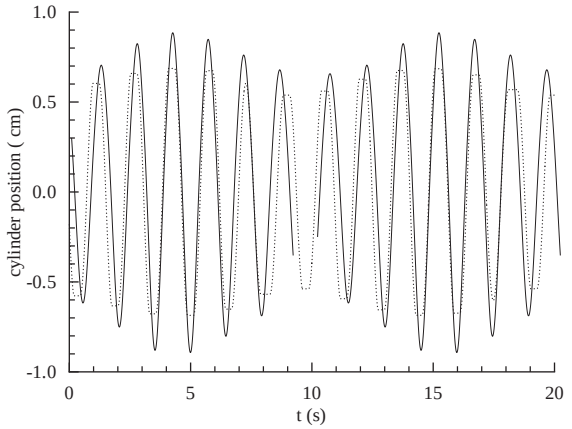

Fig. 12. Comparison of phase-averaged cylinder position vs. time measurements (solid line) with reduced-order model response (dotted line), for discrete frequencies determined from spectral peaks shown in Fig. 10.

To test this hypothesis, we used as input to the reduced-order model, simplified, single frequency functions for each of the fluid energy transport terms. We selected the dominant spectral amplitude and frequency for each of the fluid terms in Fig. 10, and used those as inputs to the model. The result of this analysis appears in Fig. 12.

Fig. 12 is again an overlay of phase-averaged measurement of cylinder position vs. time (solid line) and the reduced-order model result (dotted line). Two beating cycles are shown in the figure with the phase-averaged measurement plotted twice. While there are discrepancies between measurement and prediction, the salient feature of Fig. 12 is that the key features of the fluid–structure interaction have been captured in this simple model. The 'major' discrepancies are that the model amplitude response is somewhat smaller than the physical experiment and that the predicted oscillation frequency is slightly lower. However, errors of these types and magnitude

are not surprising owing to the fact that energy and frequency information have been discarded when employing the highly simplified energy spectra. We reiterate that the key physical response characteristics, i.e. beating, amplitude and frequency, can be quite accurately reconstructed using simplified input signals.

6. Conclusions

In summary, this paper is a report on initial successes in the development of a new paradigm for supporting reduced-order analytical modelling of fully coupled fluid–structure interactions. The long-term goal of this research is to develop a robust methodology in which highly resolved experiments provide both a priori input and a posteriori validation for key terms in the governing equations of motion. In this study, we have directly measured fluid kinetic energy transport terms to provide accurate analytic functions necessary for solving the equations of motion. By virtue of the single equation of motion, i.e. a mechanical energy equation, this particular model is useful for single degree-of-freedom problems. However, in the broader context of reduced-order modelling, the present work demonstrates the feasibility of implementing the integrated experimental/analytical modelling paradigm.

In addition to addressing modelling issues, the experimental results presented in this paper indicate that the beating behavior observed in the resonant synchronization regime results from a slight frequency mis-match between the vortex shedding frequency and cylinder oscillation frequency. Details of this finding, along with an examination of flow three-dimensionality will be developed in subsequent paper(s).

As we move forward in this research, it is obviously desirable to generalize the methodology to include fully coupled interactions with multiple degrees-of-freedom. In order to further extend McIver's principle [9] it will be necessary to include a variational approach. While this is a standard and classical tool for modelling structural dynamics, it becomes problematic when fluid continually flows across the control volume boundaries. Where one can define 'virtual displacements' subject to certain prescribed boundary constraints for a solid structure, this does not directly translate for a control volume which does not, by definition, contain the same material elements for all time. Resolving this issue will permit use of the DPIV measurements over a broader range of problems and with far greater impact.

In anticipation of generalizing this methodology, we have begun to experimentally examine two degree-of-freedom problems. In particular, we are studying the same cylinder without the cross-stream motion constraint. That is, the cylinder again moves like an inverted pendulum, but is free to vibrate in both the cross-stream and streamwise directions. Preliminary flow visualization studies have been reported in Ref. [22].

Acknowledgements

Support from the Office of Naval Research (Grant #N00014-97-1-0017) through Dr. Thomas Swean is greatly appreciated. We also acknowledge the computational support of Dr. Steven Kuchnicki in developing and running the MATLAB code for this paper.

References

[1] H. Benaroya, T. Wei, Hamilton's principle for external viscous fluid—structure interaction, *Journal of Sound & Vibration* 238 (2000) 113–145.

[2] R.I. Basu, B.J. Vickery, Across-wind vibrations of structures of circular cross-section. Part 2, Development of mathematical model for full scale application, *Journal of Wind Engineering & Industrial Aeroacoustics* 12 (1983) 75–97.

[3] E. Simiu, R.H. Scanlan, *Wind Effects on Structures*, Wiley, New York, 1986.

[4] T. Sarpkaya, Fluid forces on oscillating cylinders, *Journal of the Waterway Port Coastal & Ocean Division of the American Society of Civil Engineers* 104 (1978) 275–290.

[5] R.E.D. Bishop, A.Y. Hassan, The lift and drag forces on a circular cylinder oscillating in a flowing fluid, *Proceedings of the Royal Society of London, Series A* 277 (1963) 32–50.

[6] R.T. Hartlen, I.G. Curie, Lift-oscillator model of vortex-induced-vibration, *Journal of the Engineering Mechanics Division of the American Society of Civil Engineers* 96 (1970) 577–591.

[7] R. Landl, Theoretical model for vortex-excited oscillations, *Proceedings of the International Symposium on Vibration Problems in Industry*, 1973.

[8] W.D. Iwan, R.D. Blevins, A model for vortex-induced oscillation of structures, *American Society of Mechanical Engineers Journal of Applied Mechanics* 41 (1972) 581–586.

[9] D.B. McIver, Hamilton's principle for systems of changing mass, *Journal of Engineering Mathematics* (1973) 249–261.

[10] P. Shah, P. Atsavapranee, T.Y. Hsu, T. Wei, J. McHugh, Turbulent transport in the core of a trailing delta wing vortex, *Journal of Fluid Mechanics* 387 (1999) 151–175.

[11] T.Y. Hsu, L.M. Grega, T. Wei, R.I. Leighton, Turbulent kinetic energy transport in a corner formed by a solid wall and a free surface, *Journal of Fluid Mechanics* 410 (2000) 343–366.

[12] L.M. Grega, T.Y. Hsu, T. Wei, Transport of streamwise vorticity in a corner formed by a solid wall and a free surface, *Journal of Fluid Mechanics* 465 (2002) 331–352.

[13] A.V. Voorhees, Three-dimensionality in the Wake of a Surface-piercing Cylinder Oscillating as an Inverted Pendulum, M.S. Thesis, Department of Mechanical & Aerospace Engineering, Rutgers University, 2002.

[14] P. Atsavapranee, H. Benaroya, T. Wei, Lock-in regimes and vortex shedding modes on a freely oscillating cylinder, *American Society of Civil Engineers*; *Engineering Mechanics Division Conference*, Baltimore, MD, 1999.

[15] A. Khalak, C.H.K. Williamson, Motions, forces and mode transitions in vortex-induced vibrations at low mass-damping, *Journal of Fluids and Structures* 13 (1999) 813–851.

[16] P. Dong, Phase-averaged Transport in the Vortex-induced Oscillation of a Cylinder: Experiment and Modeling, Ph.D. Dissertation, Department of Mechanical & Aerospace Engineering, Rutgers University, 2002.

[17] M.F. Unal, J.C. Lin, D.O. Rockwell, Force prediction by PIV imaging: a momentum-based approach, *Journal of Fluids and Structures* 11 (1997) 965–971.

[18] M.S. Bloor, The transition to turbulence in the wake of a circular cylinder, *Journal of Fluid Mechanics* 19 (1964) 290–304.

[19] T. Wei, C.R. Smith, The presence of secondary vortices in the wake of circular cylinders, *Journal of Fluid Mechanics* 169 (1986) 513–533.

[20] C.H.K. Williamson, Vortex dynamics in the cylinder wake, *Annual Review of Fluid Mechanics* 28 (1996) 477–539.

[21] S.N. Kuchnicki, Analysis of the Vortex Shedding Induced Response of a Compliant Structure, Ph.D. Dissertation, Department of Mechanical & Aerospace Engineering, Rutgers University, 2001.

[22] C.M. Leong, H. Benaroya, T. Wei, Two-degree of freedom VIV of a circular cylinder pinned at one end, *Proceedings of the 2003 IUTAM Symposium on Fluid–Structure Interactions*, New Brunswick, NJ, 2–6 June 2003.